

# Effective emissivity of a cylindrical cavity with an inclined bottom: I. Isothermal cavity

Alexander V Prokhorov and Leonard M Hanssen

National Institute of Standards and Technology, 100 Bureau Drive, Gaithersburg, MD 20899, USA

E-mail: leonard.hanssen@nist.gov

Received 19 July 2004

Published 16 November 2004

Online at [stacks.iop.org/Met/41/421](http://stacks.iop.org/Met/41/421)

doi:10.1088/0026-1394/41/6/010

## Abstract

The Monte Carlo method is applied to the computation of the effective emissivity of a specular–diffuse isothermal blackbody cavity shaped by a cylindrical generatrix, a flat inclined bottom and a flat diaphragm. The dependences of the normal effective emissivity on the bottom inclination angle are studied for different cavity depths and various values of the diffuse component of the cavity wall reflectance. The distributions of the local normal effective emissivity over the cavity aperture and the dependences of the integrated effective emissivity on the distance between the aperture and the radiation detector are computed. The choice of optimal geometrical parameters for improving the radiometric performance of artificial blackbodies is discussed.

## 1. Introduction

The effective emissivity is the main figure of merit for blackbody cavities that are widely used as standard radiation sources in radiometry and radiation thermometry. Although several methods for experimental determination of the effective emissivity have been developed [1–8], most have limited areas of applicability (restricted geometry of cavity irradiation and/or reflected radiation collection, spectral range, cavity temperature, etc) and can often only be used to verify the computational model for some particular results of computations. In addition, computation of the effective emissivity remains an irreplaceable tool for blackbody design.

Among various methods that have been developed for effective emissivity calculation, the Monte Carlo method (MCM) is the most powerful and flexible. This is due to its applicability to isothermal and non-isothermal arbitrarily shaped cavities whose internal surface may have any spatial, angular and spectral distributions of emitted and reflected radiation [9]. The MCM has been successfully applied to a variety of axisymmetric cavities—conical, cylindrical and cylindro-conical [10–17], cylindrical with a re-entrant cone bottom [18], as well as cylindrical and cylindro-conical cavities

with grooved walls [19, 20]. However, on parity with the surfaces of revolution, the cylindrical cavities with an inclined (slanted or skewed) bottom are also used as blackbody radiators for temperatures in the region of 250 K to 450 K [21–27] and up to about 1400 K [28]. The European Standard [29] prescribes this shape for blackbody radiation sources intended for calibration of clinical ear thermometers.

The maxima of spectral radiance distributions of a Planckian radiator for temperatures less than 1400 K lie in the wavelength region  $>2\ \mu\text{m}$ . For many materials and coatings, the specular component of reflectance grows with wavelength in the infrared spectral range. The regular cylindrical cavity, frequently used in artificial blackbodies, has a low effective emissivity in the direction parallel to the cavity axis if the specular component of the bottom reflectance is significant. To avoid the effective emissivity decrease, the cavity bottom may have the shape of a concave or convex cone. The use of a flat inclined bottom leads to the same result, but it can be manufactured more easily.

This paper is devoted to a numerical study of the radiation characteristics of isothermal cavities having the shape of a cylinder with an inclined bottom. An algorithm for calculation of the effective emissivity for such a cavity with

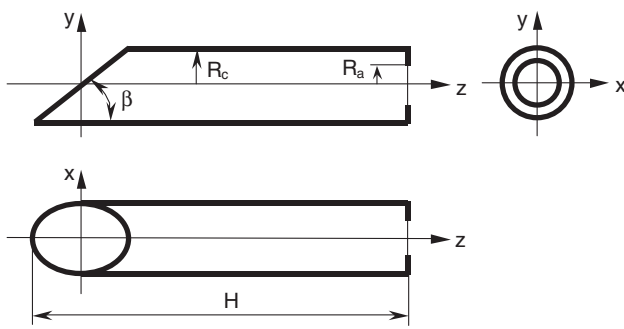


Figure 1. Drawing of a cylindrical cavity with an inclined bottom.

specular–diffuse walls is described. The results of numerical modelling using the MCM are presented and analysed.

## 2. Statement of the problem

A schematic drawing of the cavity composed of a cylindrical tube, a flat inclined bottom and a flat diaphragm is shown in figure 1. Because of the scaling properties of the problem we can use the dimensionless geometrical parameters, assuming that all of them are expressed in the same units of length. For simplicity, we set  $R_c = 1$  throughout. In order to simplify our analysis by limiting the number of affected parameters, we assume that the optical characteristics of the cavity walls are independent of the position on the cavity internal surface and wavelength (i.e. we assume that cavity internal walls are grey surfaces). Due to the cavity isothermality, we can also consider the wall emissivity to be temperature-independent. We restrict our analysis to the case of the uniform specular–diffuse reflection model that assumes the following:

- (i) The surface emits diffusely (according to Lambert’s law), with an emissivity  $\varepsilon$ .
- (ii) The hemispherical reflectance  $\rho = 1 - \varepsilon$  does not depend on the incidence angle and is a sum of two components—specular,  $\rho_s$ , and diffuse,  $\rho_d$ .
- (iii) The surface diffusivity, defined as  $D = \rho_d/\rho$ , does not depend on the incidence angle.

Moreover, we assume that the ray optics approximation is valid, that diffraction effects are negligible and that radiation is entirely depolarized due to multiple reflections.

The radiance of a Lambertian reflector is the same for all directions and does not depend on the angular distribution of the incident radiation. Because of this, the local effective emissivity, which is the primordial radiation characteristic for a cavity with purely diffuse (Lambertian) walls, is also direction-independent. According to [30], it is defined as the ratio of the wall radiosity (the sum of own thermal and reflected radiant exitances) to the radiant exitance of a perfect blackbody at the wall temperature. The spectral local effective emissivity can be defined in a similar way, using the appropriate value of the spectral radiant exitance.

The radiance of a specular–diffuse surface may vary with the direction. For a cavity having specular–diffuse, grey, isothermal walls at temperature  $T_0$ , the elementary

type of effective emissivity—spectral local directional effective emissivity—can be defined as

$$\varepsilon_e(\vec{\xi}, \vec{\omega}) = \frac{L_\lambda(\lambda, T_0, \vec{\xi}, \vec{\omega})}{L_{\lambda,bb}(\lambda, T_0)}, \quad (1)$$

where  $L_\lambda(\lambda, T_0, \vec{\xi}, \vec{\omega})$  is the spectral radiance of a cavity wall with temperature  $T_0$ , at a wavelength  $\lambda$ , at a point  $\vec{\xi}$ , in a direction  $\vec{\omega}$ ;  $L_{\lambda,bb}(\lambda, T_0)$  is the spectral radiance of a perfect blackbody determined by Planck’s law for the same wavelength and temperature.

The value of  $\varepsilon_e(\vec{\xi}, \vec{\omega})$  is independent of wavelength,  $\lambda$  (due to the spectral non-selectivity of the cavity walls), as well as of temperature (due to cavity isothermality). Similarly, the total (integrated over the entire spectrum) local directional effective emissivity can be defined through the values of radiance:

$$\varepsilon_{e,t}(\vec{\xi}, \vec{\omega}) = \frac{L(T_0, \vec{\xi}, \vec{\omega})}{L_{bb}(T_0)}, \quad (2)$$

where, according to the Stefan–Boltzmann law,  $L_{bb}(T_0) = \sigma T_0^4/\pi$ ,  $\sigma$  is the Stefan–Boltzmann constant.

For an isothermal grey cavity,  $\varepsilon_e(\vec{\xi}, \vec{\omega}) = \varepsilon_{e,t}(\vec{\xi}, \vec{\omega})$ , and a directional effective emissivity (the qualifiers ‘spectral’ and ‘total’ as well as the subscript ‘ $\lambda$ ’ can be omitted) depends only on the cavity geometry, the optical characteristics of the cavity walls and the viewing conditions.

An important special case of the local directional effective emissivity is the local normal effective emissivity,  $\varepsilon_{e,n}(x, y)$ . It corresponds to viewing the cavity aperture along an infinitely thin ray passing parallel to the cavity axis and crossing the aperture plane at the point with coordinates  $(x, y)$ . The distribution of local normal effective emissivity over a cavity aperture determines the requirements of the accuracy of the cavity and optical system alignment, as well as the uniformity of the irradiance distribution within the image of the aperture.

Another important radiometric value is the integrated effective emissivity [31, 32]. For a circular detector of radius  $R_d$  which is coaxial with a cavity and  $H_d$  distant from its aperture, the integrated effective emissivity can be defined as the ratio of the spectral radiant flux,  $\Phi_\lambda$ , or total radiant flux,  $\Phi$ , falling onto the black detector irradiated by the isothermal cavity at the temperature  $T_0$  to the spectral radiant flux,  $\Phi_{\lambda,bb}$ , or total radiant flux,  $\Phi_{bb}$ , falling onto the same detector irradiated by a perfectly black disc that substitutes the cavity aperture and has the same temperature,  $T_0$ :

$$\varepsilon_{\lambda e}(R_d, H_d) = \frac{\Phi_\lambda(\lambda, T_0, R_d, H_d)}{\Phi_{\lambda,bb}(\lambda, T_0, R_d, H_d)}, \quad (3)$$

$$\varepsilon_e(R_d, H_d) = \frac{\Phi(T_0, R_d, H_d)}{\Phi_{bb}(T_0, R_d, H_d)}. \quad (4)$$

These values can be derived from equations (2) and (3) by integration over appropriate areas and solid angles. For a grey isothermal cavity,  $\varepsilon_{\lambda e}(R_d, H_d) = \varepsilon_e(R_d, H_d)$ , and the subscript ‘ $\lambda$ ’ can be omitted.

The average normal effective emissivity,  $\varepsilon_{e,n}$ , which is used in typical calibration arrangements, can be considered as a limiting case of the integrated effective emissivity when the

detector radius,  $R_d$ , is equal to the cavity aperture radius,  $R_a$ , and  $H_d \rightarrow \infty$ . Then the following relationship exists:

$$\varepsilon_{e,n} = \frac{1}{S_a} \int_{S_a} \varepsilon_{e,n}(x, y) dS_a, \quad (5)$$

where  $S_a$  is the surface subtended by the cavity aperture.

If  $R_d = R_a$  and  $H_d = 0$ , we deal with the hemispherical effective emissivity,  $\varepsilon_{e,h}$ , which characterizes the overall radiative heat loss through the cavity aperture.

In this work, the MCM is applied to a numerical parametric study of the dependences of the effective emissivity of an isothermal cylindrical cavity with an inclined bottom on the geometrical parameters of the cavity and the optical characteristics of its walls for various viewing conditions.

### 3. Ray-tracing algorithm and program implementation

The basis of the MCM employed is the backward ray-tracing technique. As shown in [33], forward ray tracing (from within the cavity to the detector) is inefficient for integrated effective emissivity computation, and unsuited to computation of the directional effective emissivity. The suitable alternative is backward ray tracing, where the natural direction of ray propagation is reversed. This is the correct procedure if reciprocity of the wall reflectance is obeyed.

A pseudo-random number generator that produces pseudo-random numbers uniformly distributed over the interval (0, 1] is an essential component of every Monte Carlo algorithm. We use the so-called Mersenne Twister generator [34] that provides a very large period, multidimensional equidistribution, and up to 32-bit accuracy of the generated sequence.

For calculation of the local directional effective emissivity, rays are launched into the cavity along the viewing direction and reflect from the walls until they escape the cavity or until their energy become negligibly small. Upon each reflection, the type of reflection is selected: if the next pseudo-random number  $u < D$ , we consider the reflection as diffuse, and specular otherwise.

To generate the random direction of diffuse reflection, the following relationships [35] are usually employed for the zenith angle,  $\theta$ , and the azimuth angle,  $\phi$ , of the local spherical coordinate system:

$$\theta = \arcsin \sqrt{u_1}, \quad \phi = 2\pi u_2, \quad (6)$$

where  $u_1$  and  $u_2$  are a pair of pseudo-random numbers. The angular coordinates,  $\theta$  and  $\phi$ , should be transformed into Cartesian coordinates ( $\omega_{rx}, \omega_{ry}, \omega_{rz}$ ) of the reflection direction vector,  $\vec{\omega}_r$ .

We apply another algorithm based on Marsaglia's algorithm [36] for generating points uniformly distributed on the spherical surface. The algorithm's key idea is based on the fact that for perfectly diffuse reflection, the sphere with its centre at the reflection point is a surface of constant irradiation. Two pseudo-random numbers  $u_1$  and  $u_2$  after the linear transformations

$$\omega_x = 2u_1 - 1 \quad (7)$$

and

$$\omega_y = 2u_2 - 1 \quad (8)$$

are accepted if  $s = \omega_x^2 + \omega_y^2 < 1$  (the point lies inside the circle of unit radius) and rejected otherwise. If they are accepted,

$$\omega_z = \sqrt{1 - s}. \quad (9)$$

This method is up to 20% faster than the conventional method [35].

The direction of specular reflection,  $\vec{\omega}_r$ , is a deterministic value; it can be found from

$$\vec{\omega}_r = \vec{\omega}_i - 2(\vec{n} \cdot \vec{\omega}_i)\vec{n}, \quad (10)$$

where  $\vec{\omega}_i$  and  $\vec{n}$  are vectors of the direction of incidence and the normal to the surface at the incidence point, respectively.

The radiance that is observed along the  $i$ th ray from outside the isothermal cavity is equal to

$$\begin{aligned} L_i &= \varepsilon \frac{\sigma T_0^4}{\pi} + \rho \left( \varepsilon \frac{\sigma T_0^4}{\pi} + \rho \left( \varepsilon \frac{\sigma T_0^4}{\pi} + \rho(\dots) \right) \right) \\ &= \varepsilon \frac{\sigma T_0^4}{\pi} \sum_{k=1}^{m_i} \rho^{k-1}, \end{aligned} \quad (11)$$

where  $m_i$  is the number of reflections of the  $i$ th ray.

After dividing equation (11) by the radiance of a perfect blackbody at the temperature  $T_0$ ,

$$L_{bb} = \frac{\sigma T_0^4}{\pi}, \quad (12)$$

and averaging over a large number  $n$  of rays, we obtain the following simple estimator for the local directional effective emissivity:

$$\varepsilon_e(\vec{\xi}, \vec{\omega}) = \frac{\varepsilon}{n} \sum_{i=1}^n \sum_{k=1}^{m_i} \rho^{k-1}. \quad (13)$$

The same result is obtained when the spectral radiance is used.

For the hemispherical effective emissivity computation and for small distances between the aperture and the detector, we use the simplest algorithm of backward ray tracing described in [33]. It consists of generation of rays emitted diffusely by the detector surface. The rays hitting the cavity aperture are traced into the cavity; the others are rejected. This algorithm ensures fast convergence when the majority of rays hit the aperture. For larger distances between the aperture and detector, where the ray energy losses exceed 10%, we employ a more powerful algorithm that is described below.

Radiative heat transfer from a cavity aperture area  $S_a$  to the detector surface area  $S_d$  (see figure 2) is expressed by the double surface integral

$$\Phi(R_d, H_d) = \int_{S_a} \int_{S_d} \frac{L \cos^2 \psi}{d^2} dS_d dS_a, \quad (14)$$

where  $L$  is the radiance of point P in the direction  $\vec{PQ}$ .

We evaluate  $\Phi(R_d, H_d)$  by launching rays from random points  $Q_i$  distributed uniformly over the detector surface,  $S_d$ , and passing through random points  $P_i$  distributed uniformly over the flat circular area,  $S_a$ , of the cavity opening. Then every ray is directed into the cavity, and modelling of its

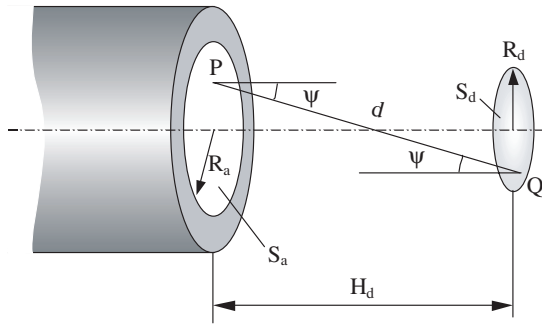


**Figure 2.** Schematic for the integrated effective emissivity calculation.

further trajectory is performed as for the directional effective emissivity. If  $L_i$  is the radiance of a ray  $Q_iP_i$ , then the estimator of radiant flux transferred from inside the cavity to the detector is equal to

$$\Phi(R_d, H_d) = \frac{S_d S_a}{n} \sum_{i=1}^n \frac{L_i \cos^2 \psi_i}{d_i^2}. \quad (15)$$

Replacing the cavity aperture with a perfectly black disc with uniform temperature  $T_0$ , we can write the analytical expression

$$\Phi_{bb}(R_d, H_d) = S_a F_{a-d} \sigma T_0^4, \quad (16)$$

where

$$F_{a-d} = \frac{1}{2} \left( Z - \sqrt{Z^2 - 4 \left( \frac{X}{Y} \right)^2} \right) \quad (17)$$

is the configuration factor from the disc area,  $S_a$ , to a coaxial disc of area  $S_d$  [35],

$$X = \frac{R_a}{H_d}, \quad Y = \frac{R_d}{H_d} \quad \text{and} \quad Z = 1 + \frac{1 + Y^2}{X^2}.$$

After dividing equation (15) by (16) and substituting equation (11), we obtain the expression for the integrated effective emissivity estimator:

$$\varepsilon_e(R_d, H_d) = \frac{S_d \varepsilon}{n \pi F_{a-d}} \sum_{i=1}^n \sum_{k=1}^{m_i} \frac{\rho^{k-1} \cos^2 \psi_k}{d_k^2}. \quad (18)$$

In order to compute the average normal effective emissivity, we employ the same algorithm as for the local normal effective emissivity (see equation (13)), except that rays hit the aperture at points that are uniformly distributed over the circular aperture area  $S_a$ .

The algorithms described are implemented in a program working on a PC under a 32-bit MS Windows operating system<sup>1</sup>. Every ray trajectory is tracked until its energy is reduced to  $10^{-5}$  of its initial value. For obtaining one effective emissivity value,  $10^7$  rays are traced to ensure that the standard deviation of the result is less than  $2 \times 10^{-5}$  in most cases.

The program has been partially (not completely due to the lack of published data) verified by comparison with

<sup>1</sup> Certain commercial software are identified in this paper in order to specify the computational procedure adequately. Such identification is not intended to imply recommendation or endorsement by the National Institute of Standards and Technology, nor is it intended to imply that the software identified are necessarily the best available for the purpose.

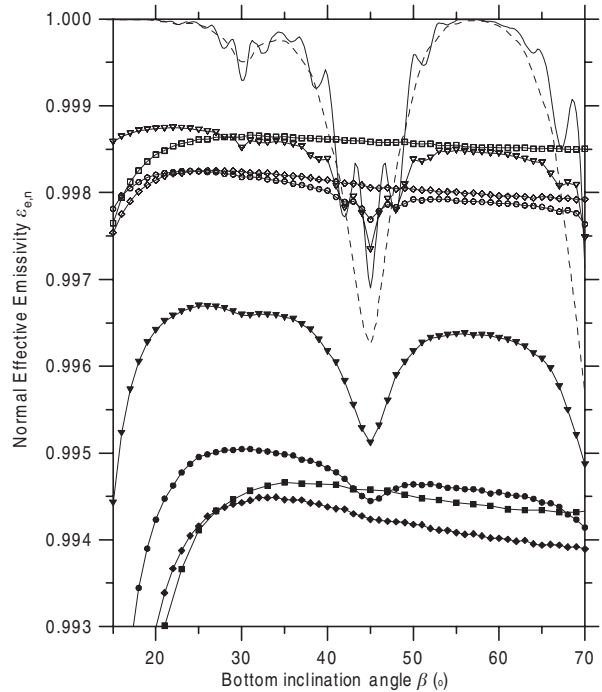


**Figure 3.** The average normal effective emissivity as a function of bottom inclination angle,  $\beta$ , for  $R_a = 0.5$  at  $D = 0$  (—),  $0.25$  ( $\nabla$ ),  $0.5$  ( $\circ$ ),  $0.75$  ( $\diamond$ ), and  $1$  ( $\square$ );  $R_a = 1$  at  $D = 0$  (---),  $0.25$  ( $\blacktriangledown$ ),  $0.5$  ( $\bullet$ );  $0.75$  ( $\blacklozenge$ ) and  $1$  ( $\blacksquare$ ).  $R_c = 1$ ,  $H = 8$ ;  $\varepsilon = 0.7$  everywhere.

results obtained by various researchers [31, 32, 37, 38] for the integrated (including hemispherical and average normal) effective emissivity of diffuse cylindrical cavities. Our results are in very good agreement with [31, 37, 38] (the discrepancies do not exceed 0.0001–0.0002; the results of these authors have similar uncertainties). Reference [32] gives values of the integrated effective emissivity for  $H_d \leq 5R_c$  greater by up to 0.002 than those of other authors. Perhaps it is due to the inaccuracy in [32] of the penumbra effect calculation. Moreover, we obtain very small random discrepancies with the results of [33] for specular–diffuse cylindrical cavities, not exceeding  $2 \times 10^{-5}$ .

## 4. Results of numerical experiments

### 4.1. Average normal effective emissivity

In the first stage of an artificial blackbody design, the radiometric performance of the isothermal cavity must be evaluated. The common task solved here is the selection of optimal cavity geometrical parameters to emulate closely the radiation properties of a perfect blackbody. The radiating cavities described in [12–16] have  $H/R_c$  ratios ranging approximately from 5 to 11. The bottom inclination angle,  $\beta$ , is equal to  $30^\circ$  in each reference.

The computed dependences of the average normal effective emissivity,  $\varepsilon_{e,n}$ , on the angle  $\beta$  for cavities having  $\varepsilon = 0.7$ ,  $R_c = 1$ ,  $H = 8$ , with and without a diaphragm ( $R_a = 0.5$  and  $R_a = 1$ ) are plotted in figure 3 for five values of the diffusivity,  $D$ . As is expected, all normal effective emissivity curves for  $D < 1$  have minima of various depths near the angle

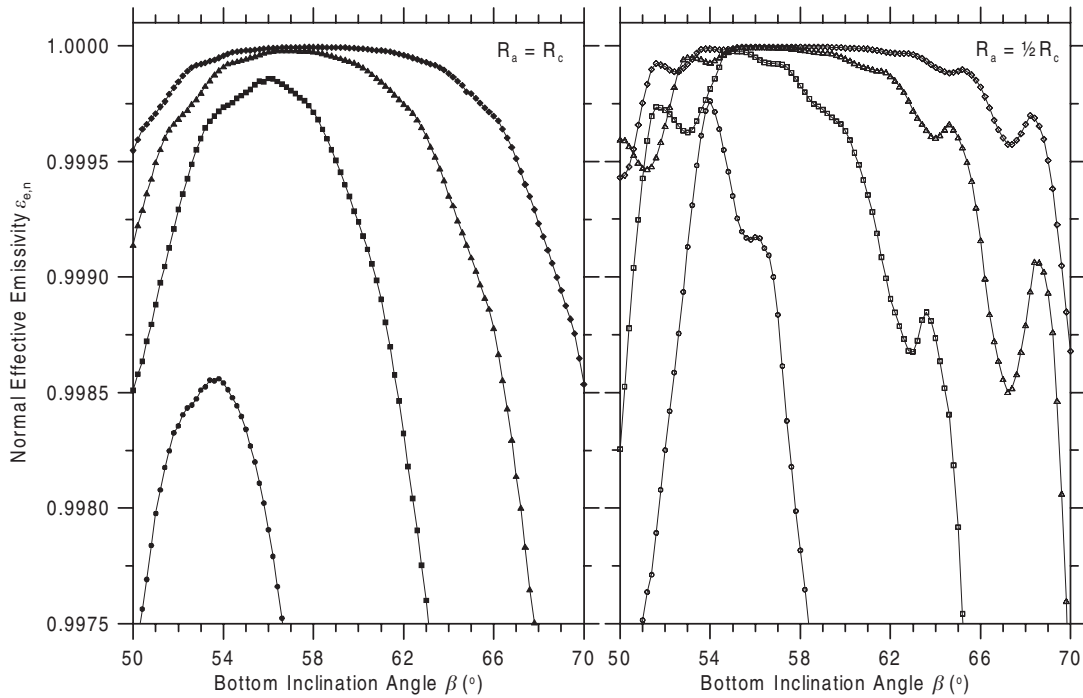


**Figure 4.** The average normal effective emissivity as a function of bottom inclination angle,  $\beta$ . Left graph:  $R_a = 1$ ;  $H = 4$  ( $\bullet$ ),  $6$  ( $\blacksquare$ ),  $8$  ( $\blacktriangle$ ),  $10$  ( $\blacklozenge$ ). Right graph:  $R_a = 0.5$ ;  $H = 4$  ( $\circ$ ),  $6$  ( $\square$ ),  $8$  ( $\triangle$ ),  $10$  ( $\diamond$ ).  $R_c = 1$  and  $\varepsilon = 0.7$  everywhere.

$\beta$ , which can ensure no more than one, two, etc reflections for most of the traced rays. So, the deep minimum at  $45^\circ$  corresponds to three reflections before escape from the cavity for every ray entering into the cavity parallel to the normal to its aperture. These minima become more smooth and less deep as the diffusivity,  $D$ , increases. The use of an aperture diaphragm is a well-known method of increasing the effective emissivity of a cavity. Together with the increase in all effective emissivity values, the curves for non-diffuse cavities acquire new minima of different depths, which correspond to the additional reflections from the diaphragm. However, the use of an aperture diaphragm does not always lead to effective emissivity growth. For example, the normal effective emissivity of a specular cavity with  $\beta = 30^\circ$  and  $R_a = 0.5$  is less than that of the same cavity without a diaphragm. This anomaly will be explained later, after analysis of the distributions of the local normal effective emissivity over the aperture.

One of the secondary minima in figure 3 corresponds to  $\beta = 30^\circ$ . The preferences of cavity designers may be conditioned by the fact that for purely specular reflecting cavity walls, this angle assures five reflections of a ray entering a cavity parallel to its axis and lying in the cavity axial plane, and all reflection points are arranged on the cavity bottom and adjacent area of the cylindrical wall. Theoretically, the choice of  $\beta = 30^\circ$  for a cavity with purely specular walls, in the presence of temperature non-uniformity, allows the developers to concentrate their efforts on ensuring isothermal conditions for only the cavity bottom and adjoining areas. We shall consider this question in more detail in a following paper. However, the ray that is not in the axial plane, after multiple reflections might have reflection points outside this zone.

For maximum  $\varepsilon_{e,n}$ , the range of  $\beta$  around  $54^\circ$ – $60^\circ$  also looks very attractive. The dependences  $\varepsilon_{e,n}(\beta)$  for

$50^\circ < \beta < 70^\circ$ ,  $\varepsilon = 0.7$ ,  $D = 0$  and four values of the cavity depth,  $H$ , are shown in figure 4. The left-hand graph is plotted for a cavity with no diaphragm, the right-hand one for one with a diaphragm of radius  $R_a = \frac{1}{2}R_c$ . Note that the locations of the maxima for opened and diaphragmed cavities are approximately coincident; they shift towards larger  $\beta$  and become flatter with increasing  $H$ .

The values of  $\varepsilon_{e,n}$  computed for various combinations of critical parameters are presented in table 1. In every column on the right of each  $D$  value there are two values of  $\varepsilon_{e,n}$ : the upper one is for  $\beta = 30^\circ$  and the lower one is for the recommended values of  $\beta$  indicated in the column header. As it is possible to see from this table, there are parameter combinations for which the lower value is greater than that for  $\beta = 30^\circ$ . The bottom inclination angle of  $30^\circ$  is better for very short cavities with preferentially specular wall reflectance and for deep cavities with preferentially diffuse wall reflectance.

#### 4.2. Local normal effective emissivity

For a cavity with specular walls, the local normal effective emissivity can be expressed by the simple formula

$$\varepsilon_{e,n}(x, y) = 1 - (1 - \varepsilon)^{m(x,y)}, \quad (19)$$

where  $m(x, y)$  is the number of successive reflections (before escaping a cavity) of a ray which enters into the cavity aperture plane at a point with coordinates  $(x, y)$  and parallel to the cavity axis.

In figure 5, the maps of the aperture section zones, which correspond to a certain number of reflections, are depicted for a specular cavity without a diaphragm,  $R_c = 1$ ,  $H = 8$ ,  $\beta = 30^\circ$  (left map) and  $58^\circ$  (right map). Due to the bilateral symmetry

**Table 1.** Average normal effective emissivities  $\varepsilon_{e,n}$  computed for various combinations of affected parameters.

$\varepsilon$	$D$	$H = 4; \beta = \begin{cases} 30^\circ \\ 54^\circ \end{cases}$		$H = 6; \beta = \begin{cases} 30^\circ \\ 56^\circ \end{cases}$		$H = 8; \beta = \begin{cases} 30^\circ \\ 58^\circ \end{cases}$		$H = 10; \beta = \begin{cases} 30^\circ \\ 60^\circ \end{cases}$		
		$R_a = 1$	$R_a = 0.5$	$R_a = 1$	$R_a = 0.5$	$R_a = 1$	$R_a = 0.5$	$R_a = 1$	$R_a = 0.5$	
0.7	0	0.999 13	0.998 89	0.999 38	0.999 14	0.999 51	0.999 30	0.999 59	0.999 39	
		0.998 54	0.999 76	0.999 86	0.999 95	0.999 98	0.999 99	0.999 99	0.999 99	
	0.25	0.984 33	0.994 69	0.993 64	0.997 47	0.996 58	0.998 51	0.997 88	0.999 01	
		0.986 94	0.995 11	0.993 76	0.997 46	0.996 36	0.998 47	0.997 63	0.998 98	
	0.5	0.972 48	0.991 61	0.989 98	0.996 57	0.995 04	0.998 17	0.997 08	0.998 88	
		0.979 20	0.992 55	0.990 38	0.996 37	0.994 58	0.997 91	0.996 55	0.998 64	
	0.75	0.962 97	0.989 58	0.987 89	0.996 38	0.994 43	0.998 24	0.996 89	0.998 97	
		0.974 54	0.991 66	0.988 99	0.996 32	0.994 06	0.997 98	0.996 31	0.998 73	
	1	0.955 27	0.988 60	0.986 98	0.996 80	0.994 53	0.998 64	0.997 10	0.999 27	
		0.972 47	0.992 19	0.989 07	0.997 06	0.994 39	0.998 52	0.996 62	0.999 13	
	0.8	0	0.999 90	0.999 85	0.999 93	0.999 89	0.999 94	0.999 91	0.999 95	0.999 93
			0.999 78	0.999 98	0.999 99	1.000 00	1.000 00	1.000 00	1.000 00	1.000 00
0.25		0.991 69	0.997 47	0.997 05	0.998 96	0.998 52	0.999 43	0.999 12	0.999 65	
		0.993 73	0.997 72	0.997 10	0.998 88	0.998 35	0.999 34	0.998 93	0.999 57	
0.5		0.984 63	0.995 61	0.994 93	0.998 39	0.997 59	0.999 18	0.998 60	0.999 51	
		0.989 20	0.996 30	0.995 17	0.998 28	0.997 31	0.999 03	0.998 29	0.999 37	
0.75		0.978 51	0.994 24	0.993 42	0.998 15	0.997 03	0.999 11	0.998 33	0.999 49	
		0.985 89	0.995 57	0.994 03	0.998 10	0.996 76	0.998 97	0.997 98	0.999 35	
1		0.973 14	0.993 35	0.992 48	0.998 18	0.996 79	0.999 22	0.998 27	0.999 57	
		0.983 75	0.995 45	0.993 50	0.998 28	0.996 58	0.999 12	0.997 90	0.999 46	
0.9		0	0.999 99	0.999 99	0.999 99	0.999 99	0.999 99	0.999 99	0.999 99	0.999 99
			0.999 98	0.999 99	0.999 99	0.999 99	0.999 99	0.999 99	0.999 99	0.999 99
	0.25	0.996 60	0.999 06	0.998 94	0.999 68	0.999 49	0.999 83	0.999 70	0.999 89	
		0.997 70	0.999 23	0.998 99	0.999 64	0.999 43	0.999 80	0.999 63	0.999 87	
	0.5	0.993 45	0.998 27	0.998 03	0.999 44	0.999 10	0.999 72	0.999 48	0.999 83	
		0.995 72	0.998 65	0.998 16	0.999 41	0.998 98	0.999 67	0.999 35	0.999 79	
	0.75	0.990 51	0.997 60	0.997 27	0.999 28	0.998 78	0.999 66	0.999 31	0.999 80	
		0.994 06	0.998 23	0.997 50	0.999 27	0.998 64	0.999 60	0.999 15	0.999 74	
	1	0.987 74	0.997 04	0.996 63	0.999 21	0.998 54	0.999 64	0.999 19	0.999 79	
		0.992 64	0.997 97	0.997 01	0.999 21	0.998 39	0.999 59	0.999 00	0.999 74	

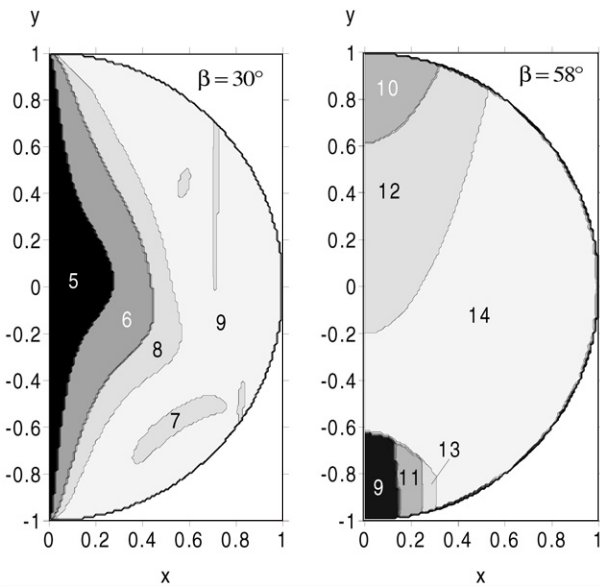


**Figure 5.** Distribution of the number of reflections for backward traced rays over the cavity aperture;  $\beta = 30^\circ$  (left map) and  $58^\circ$  (right map),  $R_a = R_c = 1$ ,  $H = 8$ ,  $\varepsilon = 0.7$ ,  $D = 0$ . Because of symmetry, only the right halves of the distributions are shown.

of the distributions, only their right halves are shown here and below.

Note that the  $YZ$  plane is the only plane of symmetry for a cavity with an inclined bottom: the bottom forms an

angle of  $30^\circ$  with a cylindrical generatrix at  $y = -R_c$ , but this angle is equal to  $60^\circ$  at  $y = R_c$ . Thus for a purely specular cavity, the rays entering into the cavity aperture through the points with coordinates  $(x, y)$  and  $(x, -y)$ , after their first reflections from the bottom, fall on the cylindrical wall at different angles. Their further trajectories will be different, so that the total number of reflections can also differ. The points on the aperture that correspond to the same number of reflections form the continuous zones of unusual shape. The zones may have irregular structure due to the three-dimensional and non-axisymmetric nature of the cavity. The shape of these zones can change when  $H$  or  $\beta$  is varied.

Three-dimensional views of the distribution of the local normal effective emissivity,  $\varepsilon_{e,n}(x, y)$ , for the same two cavities (shown in figure 5) with  $\varepsilon = 0.7$  and for  $D = 0, 0.1, 0.5$  and 1 are depicted in figure 6. The same distributions, but for cavities with a diaphragm of  $R_a = 0.5$ , are shown in figure 7.

For a cavity with purely specular walls, the distribution looks like a set of plateaus, or flat terraces having different heights and often of complicated shape. The height of every flat zone can be determined by equation (19). The presence of a relatively small diffuse component leads to a significant decrease in the distribution's step heights. At  $D = 0.5$ , the distribution relief becomes indistinct. For  $D = 1$  (purely diffuse walls), the distributions assume very smooth convex forms with minima at  $(x = 0, y = 1)$ .

Usually (but not always), the use of a diaphragm leads to a reduction in non-uniformity of the effective emissivity

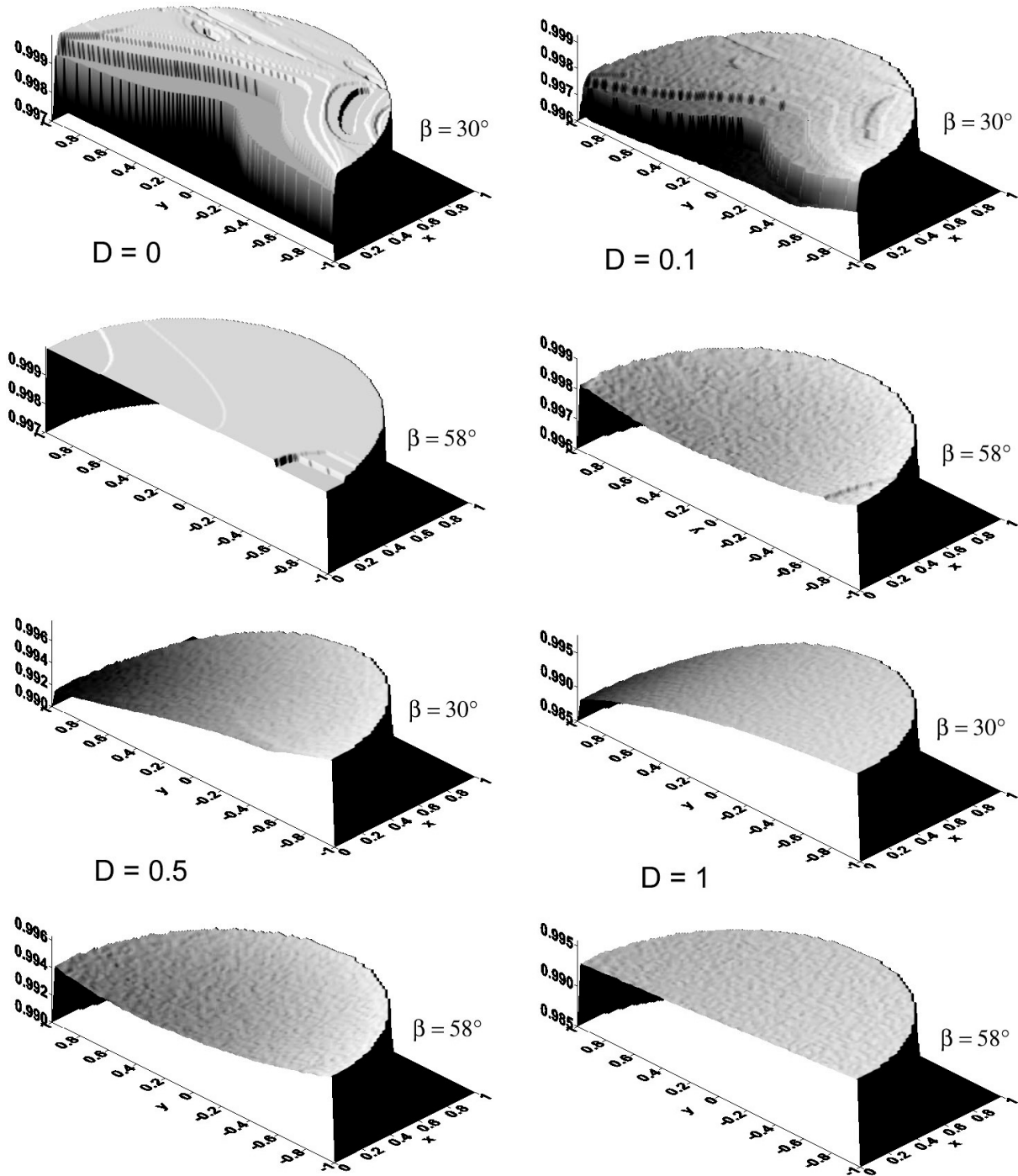


**Figure 6.** Distribution of the local normal effective emissivity over the cavity aperture for  $R_a = R_c = 1$ ,  $H = 8$ ,  $\beta = 30^\circ$  and  $58^\circ$ ,  $\varepsilon = 0.7$  and three values of diffusivity  $D$ . Because of symmetry, only the right halves of the distributions are shown.

distribution (at the expense of reduced area and radiant flux). In our case, this is correct for diffuse cavity walls. However, for a cavity with dominantly specular wall reflectance, one can observe a decrease in the average normal effective emissivity as compared with the same cavity without a diaphragm. This anomaly arises because the diaphragm excludes the high-emissivity peripheral zones of the bottom from the area of averaging.

The convergence of the Monte Carlo computational process is slower for a cavity with diffuse walls than for one

with specular walls. Therefore, the distributions for diffuse cavities have ‘rough’ surfaces whose mean height corresponds to the root-mean-square value of the random error of the computations.

#### 4.3. Integrated effective emissivity

We computed the integrated effective emissivity for  $R_d = R_a$ ,  $0 \leq H_d \leq 15$  and the same cavity as in table 1. As an example of the computed dependences, the integrated effective

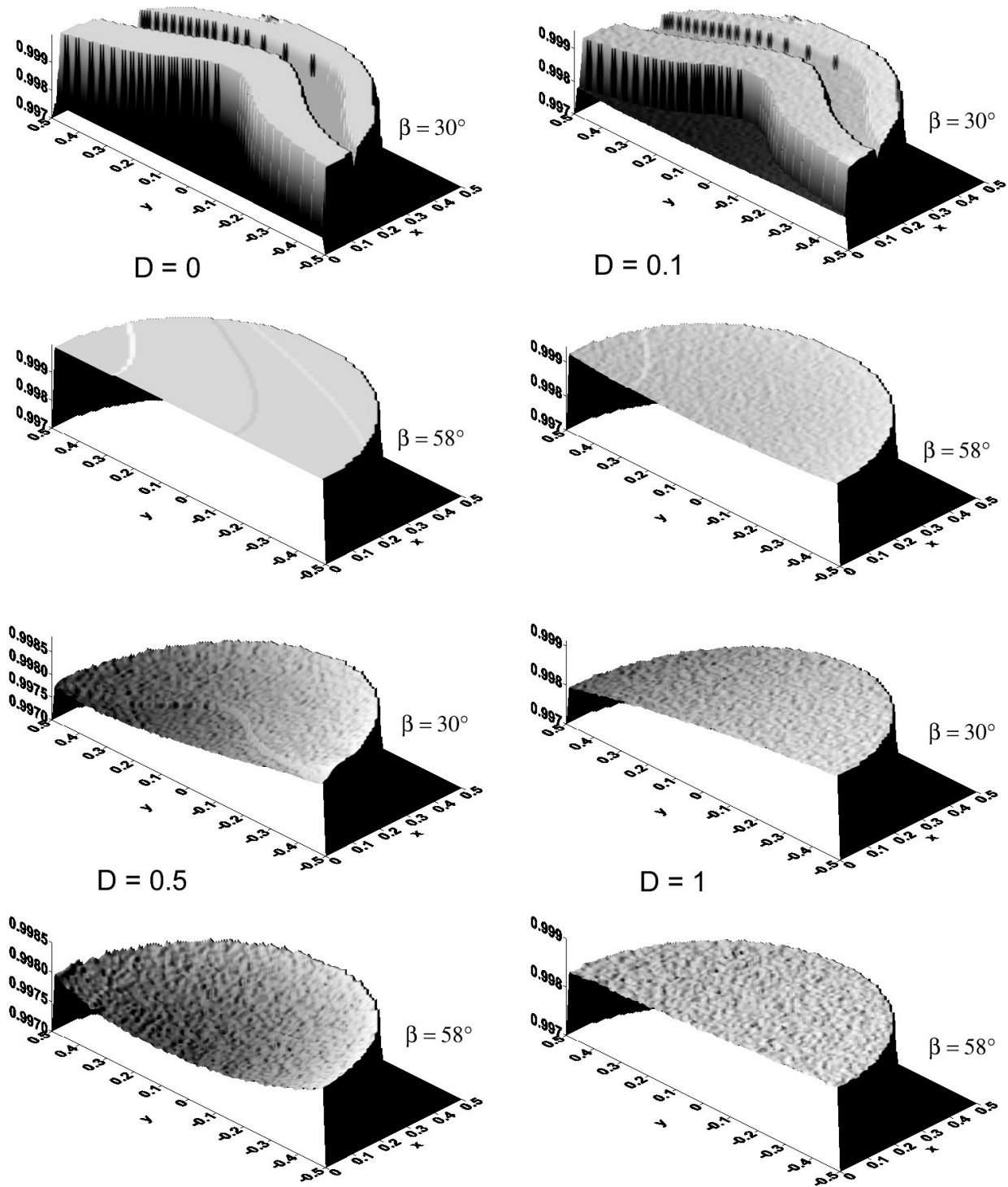


**Figure 7.** Distribution of the local normal effective emissivity over the cavity aperture for  $\beta = 30^\circ$  and  $58^\circ$ ,  $R_c = 1$ ,  $R_a = 0.5$ ,  $H = 8$ ,  $\varepsilon = 0.7$ ,  $D = 0, 0.1, 0.5$  and  $1$ . Because of symmetry, only the right halves of the distributions are shown.

emissivity of cavities having  $\beta = 30^\circ$ ,  $H = 4$ ,  $\varepsilon = 0.7$ , without a diaphragm and with a diaphragm of radius  $R_a = \frac{1}{2}R_c$ , for five values of  $D$  are plotted in figures 8 and 9 against the distance,  $H_d$ , between the cavity aperture and the detector. The analogous dependences are shown in figures 10 and 11 for a cavity having the same parameters excluding  $H = 8$ . It is assumed that the detector radius,  $R_d$ , is equal to the aperture radius,  $R_a$ , everywhere. The numerical experiments show that

in the far zone (practically for  $H_d > 10R_d$ ) the integrated effective emissivity is almost independent of  $R_d$  from the range  $(0, R_a]$ .

The integrated effective emissivity of a cavity without a diaphragm increases more slowly than that of the same cavity with a diaphragm, and at  $H_d = 15$  it is far from its asymptotic value—the normal effective emissivity,  $\varepsilon_{e,n}$ , presented in table 1.  $\varepsilon_c(R_d, H_d)$  grows with decreasing diffusivity,  $D$ , in the

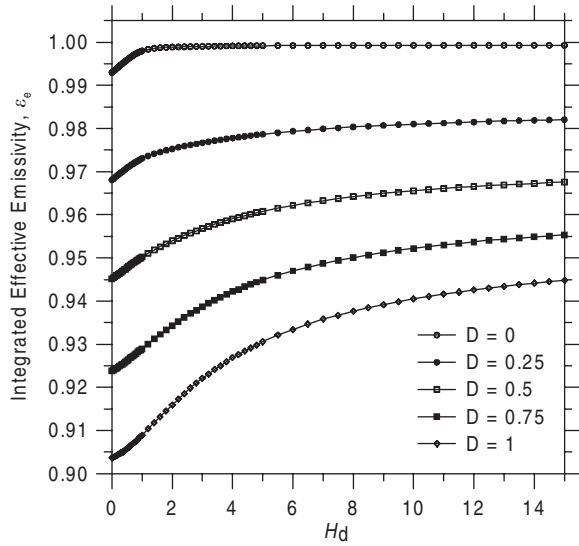


**Figure 8.** The integrated effective emissivity of a cavity without a diaphragm as a function of the distance,  $H_d$ , between the cavity aperture and the detector, for several values of diffusivity,  $D$ ;  $\beta = 30^\circ$ ,  $R_c = R_a = R_d = 1$ ,  $H = 4$  and  $\varepsilon = 0.7$ .

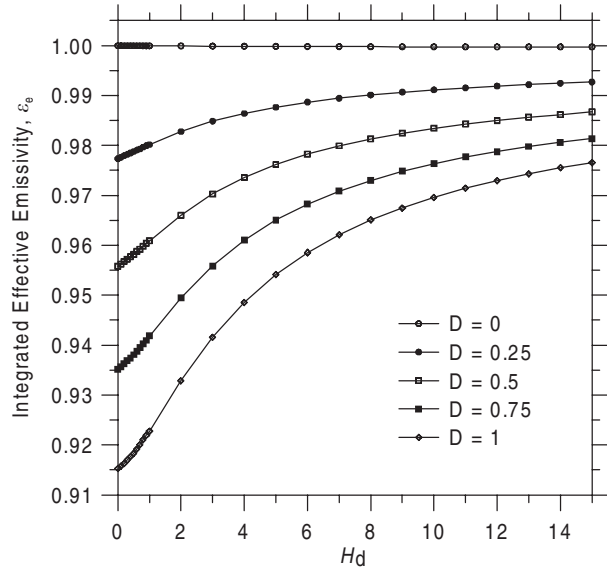


**Figure 10.** The integrated effective emissivity of a cavity without a diaphragm as a function of the distance,  $H_d$ , between the cavity aperture and the detector, for several values of diffusivity,  $D$ ;  $\beta = 30^\circ$ ,  $R_c = R_a = R_d = 1$ ,  $H = 8$  and  $\varepsilon = 0.7$ .

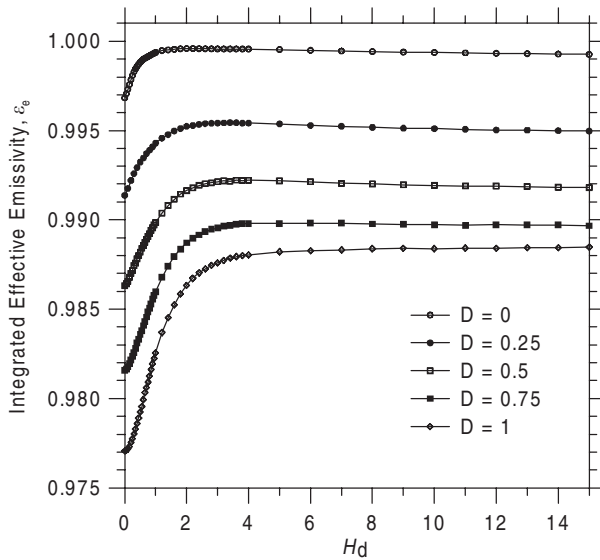


**Figure 9.** The integrated effective emissivity of a cavity with a diaphragm as a function of the distance,  $H_d$ , between the cavity aperture and the detector, for several values of diffusivity,  $D$ ;  $\beta = 30^\circ$ ,  $R_c = 1$ ,  $R_d = R_a = 0.5$ ,  $H = 4$  and  $\varepsilon = 0.7$ .

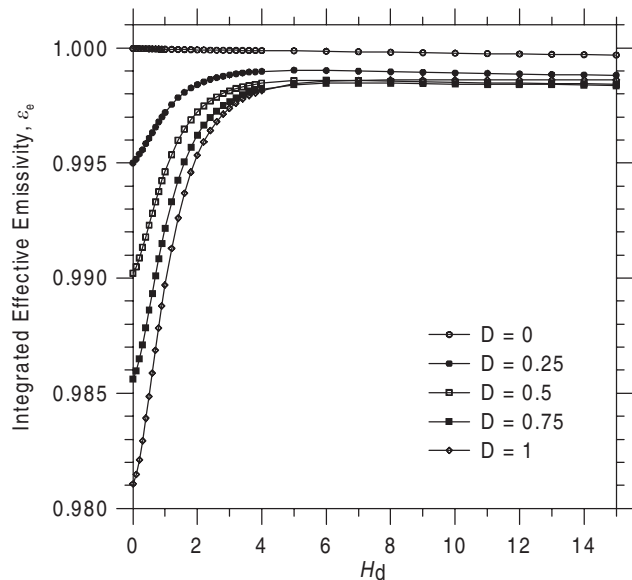


**Figure 11.** The integrated effective emissivity of a cavity with a diaphragm as a function of the distance,  $H_d$ , between the cavity aperture and the detector, for several values of diffusivity,  $D$ ;  $\beta = 30^\circ$ ,  $R_c = 1$ ,  $R_d = R_a = 0.5$ ,  $H = 8$  and  $\varepsilon = 0.7$ .

majority of cases considered, but this is not always the case. For example, if  $H_d > 7$  (see figure 11), the integrated effective emissivity of a diaphragmatic cavity with  $H = 8$  and purely diffuse walls is greater than that for  $D = 0.5$  and  $0.75$ .

#### 4.4. Hemispherical effective emissivity

$\varepsilon_e(R_d, H_d)$  at  $R_d = R_a$  and  $H_d = 0$  is the hemispherical effective emissivity,  $\varepsilon_{e,h}$ , that is necessary for exact calculation of an artificial blackbody thermal balance. Values of  $\varepsilon_{e,h}$  are presented in table 2 for the same sets of critical parameters as in table 1.

## 5. Conclusions

We have described a Monte Carlo algorithm for computing the effective emissivity of an isothermal cylindrical cavity with an inclined bottom. The results of numerical experiments can be useful for designing artificial blackbodies of such a geometry. The results obtained for the effective emissivity of an isothermal radiator may be applied to the absorption characteristics of cavity thermal detectors of optical radiation having the appropriate shape—indeed, as long as the reciprocity principle can be applied correctly.

**Table 2.** Hemispherical effective emissivities,  $\varepsilon_{e,n}$ , computed for various combinations of affected parameters.

$\varepsilon$	$D$	$H = 4; \beta = \begin{cases} 30^\circ \\ 54^\circ \end{cases}$		$H = 6; \beta = \begin{cases} 30^\circ \\ 56^\circ \end{cases}$		$H = 8; \beta = \begin{cases} 30^\circ \\ 58^\circ \end{cases}$		$H = 10; \beta = \begin{cases} 30^\circ \\ 60^\circ \end{cases}$	
		$R_a = 1$	$R_a = 0.5$	$R_a = 1$	$R_a = 0.5$	$R_a = 1$	$R_a = 0.5$	$R_a = 1$	$R_a = 0.5$
0.7	0	0.999 12	0.998 89	0.999 38	0.999 14	0.999 51	0.999 29	0.999 59	0.999 39
		0.995 96	0.998 44	0.999 45	0.999 75	0.999 89	0.999 94	0.999 97	0.999 98
	0.25	0.984 33	0.994 70	0.993 63	0.997 46	0.996 58	0.998 51	0.997 89	0.999 02
		0.973 69	0.993 72	0.976 86	0.994 83	0.977 33	0.995 01	0.977 49	0.995 05
	0.5	0.972 49	0.991 61	0.989 98	0.996 57	0.995 03	0.998 18	0.997 08	0.998 88
		0.952 49	0.989 15	0.955 37	0.990 07	0.955 85	0.990 25	0.955 97	0.990 30
	0.75	0.962 96	0.989 61	0.987 89	0.996 38	0.994 44	0.998 24	0.996 89	0.998 98
		0.932 25	0.984 69	0.934 87	0.985 48	0.935 24	0.985 61	0.935 37	0.985 66
	1	0.955 26	0.988 58	0.987 00	0.996 80	0.994 54	0.998 64	0.997 10	0.999 27
		0.912 84	0.980 32	0.915 08	0.980 99	0.915 39	0.981 08	0.915 43	0.981 10
0.8	0	0.999 90	0.999 85	0.999 93	0.999 89	0.999 94	0.999 91	0.999 95	0.999 93
		0.998 86	0.999 57	0.999 91	0.999 96	0.999 99	0.999 99	1.000 00	1.000 00
	0.25	0.991 72	0.997 46	0.997 05	0.998 96	0.998 52	0.999 43	0.999 12	0.999 65
		0.984 92	0.996 56	0.986 07	0.996 95	0.986 24	0.997 01	0.986 28	0.997 02
	0.5	0.984 64	0.995 60	0.994 93	0.998 39	0.997 58	0.999 18	0.998 60	0.999 51
		0.971 43	0.993 64	0.972 65	0.994 03	0.972 84	0.994 07	0.972 90	0.994 10
	0.75	0.978 51	0.994 25	0.993 43	0.998 15	0.997 03	0.999 11	0.998 33	0.999 49
		0.958 34	0.990 79	0.959 60	0.991 16	0.959 77	0.991 21	0.959 80	0.991 22
	1	0.973 15	0.993 36	0.992 46	0.998 19	0.996 79	0.999 22	0.998 26	0.999 57
		0.945 61	0.987 99	0.946 82	0.988 32	0.946 99	0.988 39	0.947 02	0.988 40
0.9	0	0.999 99	0.999 99	0.999 99	0.999 99	0.999 99	0.999 99	0.999 99	0.999 99
		0.999 82	0.999 93	0.999 99	0.999 99	0.999 99	0.999 99	0.999 99	0.999 99
	0.25	0.996 61	0.999 06	0.998 94	0.999 67	0.999 49	0.999 83	0.999 70	0.999 89
		0.993 32	0.998 52	0.993 60	0.998 61	0.993 63	0.998 62	0.993 63	0.998 62
	0.5	0.993 45	0.998 27	0.998 04	0.999 44	0.999 09	0.999 72	0.999 48	0.999 83
		0.986 91	0.997 14	0.987 28	0.997 25	0.987 33	0.997 26	0.987 37	0.997 26
	0.75	0.990 51	0.997 59	0.997 27	0.999 28	0.998 78	0.999 66	0.999 31	0.999 80
		0.980 62	0.995 77	0.981 03	0.995 90	0.981 11	0.995 92	0.981 13	0.995 92
	1	0.987 75	0.997 04	0.996 64	0.999 20	0.998 54	0.999 64	0.999 19	0.999 79
		0.974 39	0.994 41	0.974 88	0.994 56	0.974 95	0.994 58	0.974 98	0.994 59

We confined ourselves to the case of grey cavity walls, but the algorithm employed is also applicable to modelling spectrally-selective surfaces as was done in [13, 15]. The simple specular-diffuse model of reflection was used. However, the algorithm may be easily modified to include an arbitrary diffusivity dependence on the incidence angle as in [39]. Moreover, it is possible to incorporate in our algorithm a more realistic model of reflection, such as the perturbed normal microfacet model [40] of the bidirectional reflectance distribution function, which is both physically plausible and well suited for Monte Carlo computation.

The effect of a non-uniform wall temperature on the radiative properties of a cylindrical cavity with an inclined bottom will be evaluated in a second (II) paper.

## References

- [1] Kelly F J and Moore D G 1965 *Appl. Opt.* **4** 31–40
- [2] Heinisch R P and Schmidt R N 1970 *Appl. Opt.* **9** 1920–5
- [3] Bauer G and Bischoff K 1971 *Appl. Opt.* **10** 2639–43
- [4] Ballico M 2000 *Metrologia* **37** 295–300
- [5] Galal Yousef S, Sperfeld P and Metzendorf J 2000 *Metrologia* **37** 365–8
- [6] Ma C K 2004 *TEMPMEKO 2004: Proc. 9th Int. Symp. on Temperature and Thermal Measurements in Industry and Science (Dubrovnik, Croatia)* at press
- [7] Sakuma F and Ma L 2004 *TEMPMEKO 2004: Proc. 9th Int. Symp. on Temperature and Thermal Measurements in Industry and Science (Dubrovnik, Croatia)* at press
- [8] Mekhontsev S, Khromchenko V, Prokhorov A and Hanssen L 2004 *TEMPMEKO 2004: Proc. 9th Int. Symp. on Temperature and Thermal Measurements in Industry and Science (Dubrovnik, Croatia)* at press
- [9] Prokhorov A V 1998 *Metrologia* **35** 465–71
- [10] Heinisch R P, Sparrow E M and Shamsundar N 1973 *J. Opt. Soc. Am.* **63** 152–8
- [11] Ono A 1980 *J. Opt. Soc. Am.* **70** 547–54
- [12] Chu Z, Dai J and Bedford R E 1992 *Temperature: Its Measurement and Control in Science and Industry* vol 6, ed J F Schooley (New York: American Institute of Physics) pp 907–12
- [13] Sapritsky V I and Prokhorov A V 1992 *Metrologia* **29** 9–14
- [14] Ballico M J 1995 *Metrologia* **32** 259–65
- [15] Sapritsky V I and Prokhorov A V 1995 *Appl. Opt.* **34** 5645–52
- [16] Hartmann J, Taubert D R and Fischer J 1999 *TEMPMEKO '99: Proc. 7th Int. Symp. on Temperature and Thermal Measurements in Industry and Science* ed J F Dubbeldam and M J de Groot (Delft: NMI) pp 511–16
- [17] Nester A S and Mahan J R 2002 *Thermosense XXIV Proc. SPIE* **4710** 9–19
- [18] McEvoy H C, Machin G, Friedrich R, Hartmann J and Hollandt J 2003 *Temperature: Its Measurement and Control in Science and Industry* vol 7, ed D C Ripple (New York: American Institute of Physics) pp 909–14
- [19] Ishii J, Kobayashi M and Sakuma F 1998 *Metrologia* **35** 175–80
- [20] Té Y, Jeseck P, Camy-Peyret C, Payan S, Briaudeau S and Fanjeaux M 2003 *Metrologia* **40** 24–30
- [21] Fischer J 1999 *TEMPMEKO '99: Proc. 7th Int. Symp. on Temperature and Thermal Measurements in Industry and Science* ed J F Dubbeldam and M J de Groot (Delft: NMI) pp 27–34

- [22] Mester U and Winter P 2001 Thermosense XXIII *Proc. SPIE* **4360** 372–80
- [23] Ishii J and Ono A 2001 *Meas. Sci. Technol.* **12** 2103–12
- [24] Ishii J, Fukuzaki T, Kojima T and Ono A 2001 *TEMPMEKO 2001: Proc. 8th Int. Symp. on Temperature and Thermal Measurements in Industry and Science* vol 2, ed B Fellmuth *et al* (Berlin: PTB) pp 729–34
- [25] McEvoy H, Simpson R and Machin G 2004 Thermosense XXVI *Proc. SPIE* **5405** 54–60
- [26] Ishii J, Fukuzaki T, McEvoy H C, Simpson R, Machin R, Hartmann J, Gutschwager B and Hollandt J 2004 *TEMPMEKO 2004: Proc. 9th Int. Symp. on Temperature and Thermal Measurements in Industry and Science (Dubrovnik, Croatia)* at press
- [27] Pušnik I, van der Ham E and Drnovšek J 2004 *TEMPMEKO 2004: Proc. 9th Int. Symp. on Temperature and Thermal Measurements in Industry and Science (Dubrovnik, Croatia)* at press
- [28] Dril A, Nasibov H and Uğur S 2003 *Temperature: Its Measurement and Control in Science and Industry* vol 7, ed D C Ripple (New York: American Institute of Physics) pp 663–8
- [29] European Standard EN 12470-5:2003 2003 *Clinical Thermometers—Part 5: Performance of Infrared Ear Thermometers (with Maximum Device)* CEN TC205 p 29
- [30] Bedford R E and Ma C K 1974 *J. Opt. Soc. Am.* **64** 339–49
- [31] Chen S, Chu Z and Chen H 1980 *Metrologia* **16** 69–72
- [32] Chu Z, Bedford R E, Xu W and Liu X 1989 *Appl. Opt.* **28** 1826–9
- [33] Prokhorov A, Mekhontsev S and Hanssen L 2003 *Temperature: Its Measurement and Control in Science and Industry* vol 7, ed D C Ripple (New York: American Institute of Physics) pp 729–34
- [34] Matsumoto M and Nishimura T 1998 *ACM Trans. Modeling Comput. Simul.* **8** 3–30
- [35] Siegel R and Howell J R 2002 *Thermal Radiation Heat Transfer* 4th edn (London: Taylor and Francis)
- [36] Marsaglia G 1972 *Ann. Math. Stat.* **43** 645–6
- [37] Chandos R J and Chandos R E 1974 *Appl. Opt.* **13** 2142–52
- [38] Ohwada Y 1984 *Japan. J. Appl. Phys.* **23** L167–8
- [39] Prokhorov A V, Mekhontsev S N and Hanssen L M 2003/2004 *High Temp.—High Press.* **33–36** 199–207
- [40] Prokhorov A V and Hanssen L M 2003 *Proc. SPIE* **5192** 141–57

# Erratum

## Effective emissivity of a cylindrical cavity with an inclined bottom: I. Isothermal cavity

Alexander V Prokhorov and Leonard M Hanssen 2004

*Metrologia* 41 421–431

In table 2 of this paper, the values of the normal effective emissivity are presented, instead of values of the hemispherical effective emissivity for an isothermal cavity with  $\beta = 30^\circ$ . Here, we present the corrected portion of table 2. Also, in figure 5 (right-side plot) and figure 6 (left column, second row), instead of a cavity with  $\beta = 58^\circ$ , the plots for a cavity with slightly different geometric parameters are shown. We show here the corrected map of reflections and a three-dimensional plot of the distribution of the local normal effective emissivity.

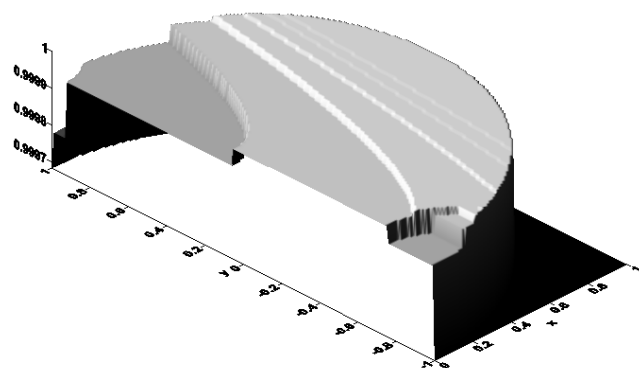


**Figure 6.** (left column, second row) Distribution of the local normal effective emissivity over the aperture of an isothermal cavity with  $R_c = R_a = 1$ ,  $H = 8$ ,  $\beta = 58^\circ$ ,  $\varepsilon = 0.7$  and  $D = 0$ .

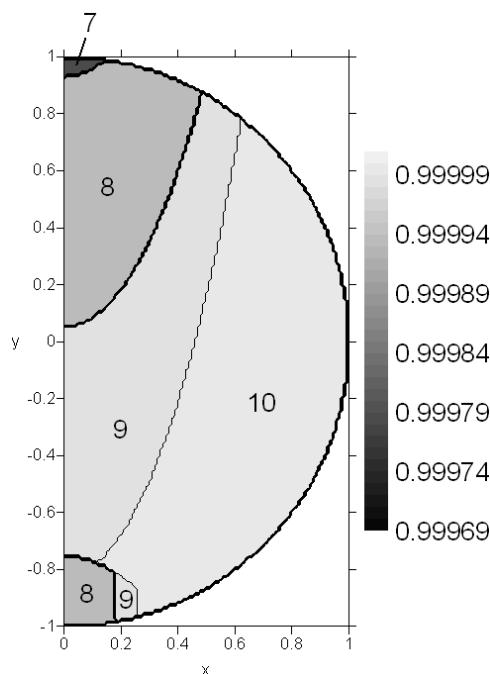


**Figure 5.** (right-side plot) Number of reflections map for a cavity with  $R_c = R_a = 1$ ,  $H = 8$ ,  $\beta = 58^\circ$  and  $D = 0$ . Figures inside the shaded areas denote the number of reflections for backward ray tracing of the rays that are parallel to the cavity axis.

**Table 2.** (corrected portion) Hemispherical effective emissivity,  $\varepsilon_{e,h}$ , computed for isothermal cavity with  $\beta = 30^\circ$  and various combinations of parameters  $R_a$ ,  $H$ ,  $\varepsilon$  and  $D$ .

$\varepsilon$	$D$	$H = 4$		$H = 6$		$H = 8$		$H = 10$	
		$R_a = 1$	$R_a = 0.5$						
0.7	0	0.99299	0.99682	0.99981	0.99991	0.99996	0.99998	0.99998	0.99999
	0.25	0.96808	0.99133	0.97667	0.99478	0.97734	0.99498	0.97748	0.99506
	0.5	0.94516	0.98631	0.95492	0.98994	0.95572	0.99021	0.95603	0.99028
	0.75	0.92372	0.98159	0.93426	0.98532	0.93514	0.98561	0.93537	0.98565
	1	0.90362	0.97708	0.91452	0.98079	0.91527	0.98104	0.91551	0.98112
0.8	0	0.99700	0.99851	0.99998	0.99999	1.00000	1.00000	1.00000	1.00000
	0.25	0.98177	0.99517	0.98600	0.99692	0.98622	0.99700	0.98625	0.99703
	0.5	0.96728	0.99201	0.97245	0.99395	0.97280	0.99408	0.97286	0.99410
	0.75	0.95332	0.98894	0.95927	0.99109	0.95973	0.99122	0.95984	0.99122
	1	0.94002	0.98598	0.94645	0.98824	0.94696	0.98835	0.94702	0.98840
0.9	0	0.99898	0.99945	0.99999	0.99999	0.99999	0.99999	0.99999	0.99999
	0.25	0.99199	0.99792	0.99355	0.99859	0.99363	0.99862	0.99363	0.99862
	0.5	0.98513	0.99642	0.98720	0.99723	0.98734	0.99726	0.98734	0.99727
	0.75	0.97842	0.99496	0.98094	0.99587	0.98110	0.99592	0.98115	0.99591
	1	0.97185	0.99352	0.97474	0.99452	0.97494	0.99458	0.97495	0.99458